Hybrid simulation of NBI fast-ion losses due to the Alfvén eigenmode bursts in the Large Helical Device and the comparison with the Fast-Ion-Loss Detector measurements

R. Seki[1,2]†, Y. Todo[1], Y. Suzuki[1,2], K. Ogawa[1,2], M. Isobe[1,2], D.A. Spong[3], and M. Osakabe[1,2]

[1]National Institute for Fusion Science, National Institutes of Natural Sciences, Toki, Japan

[2]The Graduate University for Advanced Studies, SOKENDAI, Toki, Japan

[3]Oak Ridge National Laboratory, Oak Ridge, USA

The multi-phase simulations are conducted with the kinetic-magnetohydrodynamics hybrid code MEGA to investigate the spatial and the velocity distributions of lost fast ions due to the Alfvén eigenmode (AE) bursts in the Large Helical Device (LHD) plasmas. It is found that fast ions are lost along the divertor region with helical symmetry both before and during the AE burst except for the promptly lost particles. On the other hand, several peaks are present in the spatial distribution of lost fast ions along the divertor region. These peaks along the divertor region can be attributed to the deviation of the fast-ion orbits from the magnetic surfaces due to the grad-B and the curvature drifts. For comparison with the velocity distribution of lost fast ions measured by the Fast-Ion-Loss Detector (FILD), the "numerical FILD" which solves Newton-Lorentz equation is constructed in the MEGA code. The velocity distribution of lost fast ions detected by the numerical FILD during AE burst is in good qualitative agreement with the experimental FILD measurements. During the AE burst, fast ions with high energy ($100 - 180$ keV) are detected by the numerical FILD while co-going fast ions lost to the divertor region is the particles with lower energy than 50 keV.

1. Introduction

The fast-ion confinement is an important issue for the prediction of the heating efficiency in a fusion reactor. The fast-ion confinement depends not only on the collisional transport in the equilibrium magnetic field but also on the fast-ion transport and losses induced by the fast-ion driven instabilities such as Alfvén Eigenmondes (AE). Therefore, it is an important challenge to clarify the fast-ion transport due to the fast-ion driven magnetohydrodynamic (MHD) instabilities.

In the Large Helical Device (LHD), which is one of the largest helical devices, fast-ion confinement has been investigated by using the three tangential neutral beam injectors (NBIs) and two perpendicular NBIs. The fast-ion driven MHD instabilities such as the Toroidal Alfvén Eigenmondes (TAEs) have been observed in the LHD experiments(Osakabe et al. 2006). In addition, the AE-induced fast-ion losses were observed by a scintillator-based fast-ion loss detector (FILD)(Ogawa et al. 2012). On the other hand, since there is a poloidal dependence of fast-ion loss in the LHD even without AE instabilities, it is difficult to get an overall understanding of fast-ion loss process

† Email address for correspondence: seki.ryohsuke@nifs.ac.jp

only by the local measurements. Computer simulation is a powerful tool to investigate the interaction between fast-ions and fast-ion driven AE instabilities such as the fast-ion transport and losses induced by the AEs.

MHD hybrid simulation models have been constructed to study the interaction between fast ions and MHD instabilities(Todo & Sato 1998; Park et al. 1992; Spong et al. 1992; Todo et al. 1995; Briguglio et al. 1995; Fu et al. 2006; Wang et al. 2010; Burby & Tronci 2017). The multi-phase MHD hybrid simulation, which is a combination of classical simulation and MHD hybrid simulation, has been developed and implemented in the MEGA code to investigate the fast ion distribution formation process with the interaction of the MHD instabilities in the collisional time scale(Todo et al. 2014). The multi-phase hybrid simulations were successfully validated with the tokamak experiments on the significantly flattened fast ion pressure profile, the electron temperature fluctuations brought about by the AEs, and the AE bursts(Todo et al. 2015, 2016; Todo 2016; Bierwage et al. 2018; Todo 2019). The MEGA code has been applied also to the LHD plasmas. Good agreement was found on the spatial profile and the growth rate of the ballooning modes between the MHD part of the MEGA code (MIPS code) and the CAS3D code(Todo et al. 2010b; Nührenberg 1999). A reduced version of MEGA, where the AE spatial profile and the frequency are given in advance of the simulation and the evolution of the AEs and the fast ions are followed self-consistently, was developed and run to investigate the AE bursts and the fast-ion transport in LHD(Todo et al. 2010a; Nishimura et al. 2013). The multi-phase hybrid simulation of the MEGA code was applied to the LHD experiments to investigate the fast-ion transport brought about by the AE bursts(Todo et al. 2017; Seki et al. 2019). The energetic-particle driven geodesic acoustic modes (EGAMs) in the LHD were simulated with MEGA. The sudden excitation of the half-frequency EGAM during the frequency chirping of the primary EGAM was reproduced, and the triggering mechanism through the nonlinear resonance overlap was discovered(Wang et al. 2018). The MEGA code has been extended with kinetic thermal ions. The energy channeling from fast ions to thermal ions through the interaction with the EGAM was demonstrated for the first time(Wang et al. 2019), and the kinetic stabilizing effect of trapped thermal ions was found on the ballooning modes in LHD(Sato & Todo 2019). The stabilizing effect of fast ions was also found on interchange modes in LHD if the initial total pressure profile is assumed to be the same for different fast ion pressure(Pinon et al. 2018).

On the other hand, the fast-ion transport and losses due to AE burst in MEGA has not been compared with the experimental results in the non-axisymmetric three-dimension magnetic configuration such as LHD. In the previous comparison of fast-ion losses due to AE burst in the LHD, the fast-ion detected by FILD were simulated by tracing fast-ion orbits with model of the AE profile(Ogawa et al. 2012). In this comparison, the increase of fast-ion loss due to the AE burst is similar to experimental results. On the other hand, the energy of lost fast ion is only near the injection energy. Therefore, we apply the multi-phase simulation to the LHD plasmas where the spatial and the velocity distribution of lost fast ions due to the AE burst was investigated with the FILD. In order to compare the MEGA simulation results with the FILD measurements, the "numerical FILD" which solves Newton-Lorentz equation has been developed and implemented in the MEGA simulation where usually the guiding-center orbits of fast ions are followed. In this work, we compare the velocity distribution of fast ions detected by "numerical FILD" with that detected by the FILD in the LHD experiment. In addition, we investigate the difference between fast ions detected by the "numerical FILD" and lost fast ions in the divertor region.

2. Simulation Model of MEGA

We use the MEGA code(Todo & Sato 1998), in which the bulk plasma is described by the nonlinear MHD equations and the fast ions are simulated with the gyrokinetic particle-in-cell (PIC) method. In this paper, we use the MHD equations with the fast-ion effects

$$\frac{\partial \rho}{\partial t} = -\nabla(\rho\boldsymbol{v}) + \nu_n\Delta(\rho - \rho_{\text{eq}}) \tag{2.1}$$

$$\rho\frac{\partial}{\partial t}\boldsymbol{v} = -\rho\boldsymbol{v}\cdot\nabla\boldsymbol{v} - \nabla p$$
$$+ (\boldsymbol{j} - \boldsymbol{j}_h)\times\boldsymbol{B} + \frac{4}{3}\nabla(\nu\rho\nabla\cdot\boldsymbol{v}) - \nabla\times(\nu\rho\boldsymbol{\omega}) \tag{2.2}$$

$$\frac{\partial p}{\partial t} = -\nabla\cdot(p\boldsymbol{v}) - (\gamma - 1)p\nabla\cdot\boldsymbol{v}$$
$$+ (\gamma - 1)\left[\nu\rho\omega^2 + \frac{4}{3}\nu\rho(\nabla\cdot\boldsymbol{v})^2 + \eta\boldsymbol{j}\cdot(\boldsymbol{j} - \boldsymbol{j}_{\text{eq}})\right]$$
$$+ \chi\Delta(p - p_{\text{eq}}) \tag{2.3}$$

$$\frac{\partial\boldsymbol{B}}{\partial t} = -\nabla\times\boldsymbol{E}, \boldsymbol{j} = \frac{1}{\mu_0}\nabla\times\boldsymbol{B} \tag{2.4}$$

$$\boldsymbol{E} = -\boldsymbol{v}\times\boldsymbol{B} + \eta(\boldsymbol{j} - \boldsymbol{j}_{\text{eq}}) \tag{2.5}$$

$$\boldsymbol{\omega} = \nabla\times\boldsymbol{v} \tag{2.6}$$

where μ_0 is the vacuum magnetic permeability, $\gamma = 5/3$ is the adiabatic constant, and ν, ν_n and χ are artificial viscosity and diffusion coefficients chosen to maintain numerical stability. In this work, the dissipation coefficients ν, ν_n, χ and η/ν_0 are assumed to be equal to each other. The dissipation terms play a physical role in enhancing the damping of AEs in the MHD simulation that does not include kinetic damping such as radiative damping(Mett & Mahajan 1992) and thermal ion Landau damping. In this paper, we use one value of the coefficients, 5×10^{-6}, normalized by $v_A R_0$, where v_A is the Alfvén velocity at the plasma center and R_0 is the major radius at the geometrical center of the simulation domain. The subscript "eq" represents the equilibrium variables. The MHD momentum equation [Eq. 2.2] includes the fast-ion current density $\boldsymbol{j}_h$that consists of the contributions from parallel velocity, magnetic curvature and gradient drifts, and magnetization current. We see that the electromagnetic field is given by the standard MHD description. This model is accurate under the condition that the fast-ion density is much less than the bulk plasma density. The MHD equations are solved using a fourth order (in both space and time) finite difference scheme. The fast-ion current density is defined as follows.

$$\boldsymbol{j}_h \equiv j_{h\parallel}\boldsymbol{b} + \frac{1}{B}\left(P_{h\parallel}\nabla\times\boldsymbol{b} - P_{h\perp}\nabla\ln B\times\boldsymbol{b}\right) - \nabla\times\left(\frac{P_{h\perp}}{B}\boldsymbol{b}\right) \tag{2.7}$$

where $j_{h\parallel}$ denotes the parallel component of the fast-ion current density. $P_{h\parallel}$ and $P_{h\perp}$ are parallel and perpendicular components of fast-ion pressure, respectively. These pressure components are calculated by using the full-f PIC method based on a guiding-center

approximation. The guiding center equations for each computational particle are solved using a fourth-order Runge-Kutta method and the linear interpolation. The $\boldsymbol{E} \times \boldsymbol{B}$ drift disappears in $\boldsymbol{j}_h$ due to quasi-neutrality(Todo & Sato 1998).

We have investigated the fast-ion distribution formation process with beam injection, collisions, losses, and transport due to the AEs. A complicating factor is that the time scale of the classical processes without MHD perturbations is the slowing-down time, which is roughly 100 ms, and longer by four orders of magnitude than the typical oscillation period of AEs ~ 0.01 ms. The time step width is limited by the Courant condition for fast magnetosonic waves in the hybrid simulation. On the other hand, in the classical simulation, where the MHD part of the simulation is turned off, the time step width can be taken to be greater by one order of magnitude than in the hybrid simulation. To deal with this efficiently, a multi-phase simulation, where the classical simulation and the hybrid simulation are run alternately, was constructed(Todo et al. 2014, 2015, 2016; Todo 2016; Bierwage & Todo 2017). In the classical phase of the simulation, the fast-ion distribution is built up with the beam injection and collisions. In the subsequent hybrid phase, the built-up fast-ion distribution destabilizes AEs leading to the relaxation of the distribution. We should note that the classical processes, beam injection and collisions, also take place in the hybrid phase. We repeat this combination of the classical and hybrid simulations until the stored fast-ion energy is saturated.

3. Fast-ion loss simulation during the TAE burst in the LHD

3.1. TAE burst and fast-ion loss

3.1.1. Simulation condition

In order to clarify the fast-ion loss process due to the TAE burst, a multi-phase simulation of MEGA code is applied to the LHD discharge #90090(Ogawa et al. 2012), in which the fast-ion losses were observed during the TAE burst. Since the time interval of TAE burst in the LHD experiment is about 5 ms, the classical simulation and the hybrid simulation are alternately run for 2 ms and 3 ms, respectively. The equilibrium magnetic field is calculated by the HINT2 code(Harafuji et al. 1989; Suzuki et al. 2006) based on the profiles of electron density and temperature measured in the LHD experiment. The magnetic field strength at the magnetic axis is 0.6T. In this experiment, three tangentially injected NBs composed of the two co-injected NBs and one counter-injected NB are used. The word "co" means that the direction of the effective toroidal current is consistent with the clockwise directed rotational transform. The word "counter" means the opposite direction. In the LHD, the "co" direction approximately corresponds to the direction of the magnetic field. The injection powers of co-injected NB and counter-injected NB are about 10 MW and 5 MW, respectively. Using the density and temperature profiles shown in Fig. 1 (a), the birth locations of fast-ions shown in Fig. 1 (b) is calculated by the HFREYA code considering the injection energy of each NB. In the simulation, the fast ions are traced from these non-axisymmetric birth locations and the fast ions with non-axisymmetric birth locations are used as the fast-ion source. The fast-ion distribution in the steady state is shown in Fig. 1 (c).

3.1.2. Time evolution of AEs and fast-ion losses

The time evolutions of MHD kinetic energy of fast-ion driven instabilities, stored fast-ion energy and lost power of fast ions due to the instabilities in the multi-phase simulation with MEGA code are shown in Fig. 2. The fast ions that reach the divertor region or the vacuum vessel are identified as lost particles. In Fig. 2(b) and (c), the results of the
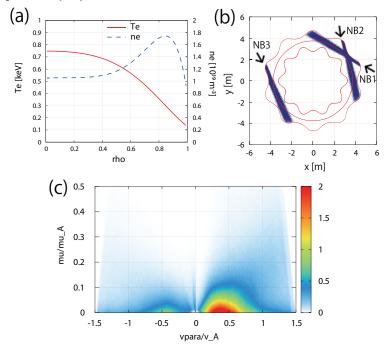
FIGURE 1. (a) Electron temperature and density profiles in the LHD discharge #90090 (b) fast-ion birth locations produced by NB and (c) fast-ion distribution. In panel (a), solid and dashed lines show the temperature and density profiles, respectively. In panel (b), blue points represent the birth points projected onto the equatorial plane. Red lines represent the last closed flux surface and the magnetic axis. In panel (c), the horizontal axis is the parallel velocity normalized by the Alfvén velocity v_A. The vertical axis is the magnetic moment normalized by $\mu_A = m v_A^2 / 2 B_{axis}$.

"classical calculation" which are the results of MEGA code without MHD instabilities, are shown for comparison. In Fig. 2(c), the lost power of fast ions does not include the promptly lost particles whose lifetime is less than 50 μs. We see in Fig. 2(a) that the recurrent bursts of fast-ion driven instabilities take place. As a result, the stored fast-ion energy is saturated at lower levels than in the "classical calculation" (Fig. 2(b)). In addition, the lost power of fast ions shown in Fig. 2(c) significantly increases during each burst of the instabilities.

Figure 3(a) and 3(b) show the spatial distributions of power density of fast ion lost to the divertor region or the vacuum vessel in the classical phase and the hybrid phase, respectively. In Fig. 3, the promptly lost particles are not included. The power density of lost fast ion in the hybrid phase shown in Fig. 3(b) is larger than that in the classical phase shown in Fig. 3(a). One can observe the helical symmetry of lost fast-ion location even in the hybrid phase because most of the lost fast ions reach the divertor region following the divertor magnetic field.

On the other hand, there are some peaks in the power density of lost fast ions along the divertor location. In order to clarify the peaks along the divertor location, the spatial distributions of the increment in the lost power of fast ions in the hybrid phase from that in the classical phase are shown for co-going fast ions in Fig. 4(a) and for counter-going fast ions in Fig. 4(b). In Fig. 4, the spatial distribution of power density is shown for $0 \leqslant \phi \leqslant 2\pi/5$ (two helical pitch). For the co-going fast ions, the power density of lost fast ions is larger in the outer side of the torus while the counter-going fast ions are mainly
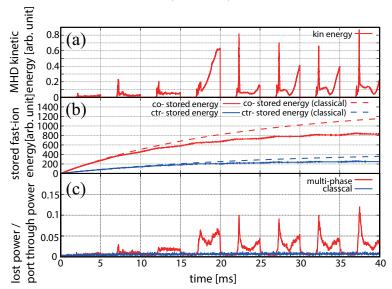
FIGURE 2. Time evolutions of (a) MHD kinetic energy of the fast-ion driven instabilities, (b) stored fast-ion energy, and (c) lost power of fast ions. In panels (b) and (c), the results of the "classical calculation", which are the results of MEGA code without MHD instabilities, are shown together for comparison. In panel (c), vertical axis is the lost power of fast ions normalized by port-through power. The lost power of fast ions does not include the promptly lost particles whose lifetime is less than 50 μs.

lost in the inner side of the torus. This tendency of fast-ion loss is consistent with the deviation of the fast-ion orbit from the magnetic surface due to the grad-B and curvature drifts.

Next, we investigate the fast-ion pressure variation during the AE burst. Figure 5 shows the time evolution of MHD kinetic energy, mode amplitudes with $m/n = 2/1$ and $m/n = 1/1$, the fast-ion pressure variation from $t = 37$ ms, and fast-ion loss rate during the typical AE burst. Here, m and n represents the poloidal mode number and the toroidal mode number, respectively. The mode amplitudes with $m/n = 2/1$ and $m/n = 1/1$ are evaluated at rho=0.3 and rho=0.1, respectively. These radial positions are near the maxima of mode amplitudes as shown in Ref. Seki et al. (2019). In Fig. 5(b), the primary mode number at the beginning of the AE burst is $m/n = 1/1$. And then, the instability with $m/n = 2/1$ becomes large in this MEGA simulation. The frequency of AE with $m/n = 2/1$ is ~ 50 kHz. The frequency is close to experiments#90090(Ogawa et al. 2012). The increase of the MHD kinetic energy for $t > 39.5$ ms is caused by low frequency MHD instabilities near peripheral region. Therefore, the mode amplitudes of AE do not increase for $t > 39.5$ ms. The detailed analyses of the AE burst were summarized in Ref. Seki et al. (2019). It is found in Fig. 5 that the fast-ion pressure profile rapidly changes at the peak of the $m/n = 2/1$ mode amplitude. The fast-ion pressure decreases for rho < 0.6 and increase for rho > 0.6. After the peak of the $m/n = 2/1$ mode amplitude, fast-ion pressure profile gradually recovers. The effect of the $m/n = 1/1$ mode on the fast-ion loss rate is weak because this mode is located near the plasma center.
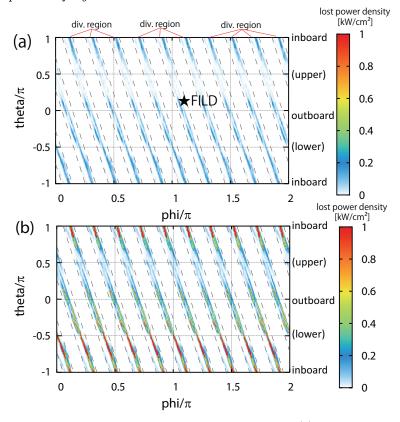
FIGURE 3. Spatial distributions of power density of lost fast ion in (a) the classical phase and (b) the hybrid phase. The horizontal and vertical axes are the toroidal angle and poloidal angle of lost fast-ion location, respectively. Color represents the power density of lost fast ion [kW/cm^2]. The promptly lost particles whose lifetime are less than 50 μs are not included.

3.2. *Validation of fast-ion loss simulation with FILD measurements*
3.2.1. *Model of numerical FILD*

In order to validate the fast-ion loss simulation with MEGA code, the velocity distribution of lost fast ions calculated by MEGA is compared with that measured by FILD. In the FILD in the LHD experiments, the velocity distribution of the co-going fast ions lost due to AE burst is observed. Here, the "numerical FILD" has been developed in order to compare the MEGA simulation with the FILD measurements. In the numerical FILD, the position of the probe and the aperture is set in accordance with the FILD installation position. The aperture shape of the numerical FILD is a circle with radius 6 mm. The aperture size of the numerical FILD is set about 5 times larger than that of the actual FILD in order to reduce the Monte Carlo error by increasing the number of fast ions detected with the numerical FILD. In the numerical FILD, fast ions near the installation position of the FILD are retraced along the full orbit following Newton-Lorentz equation. In the standard MEGA simulation, the guiding-center orbits of fast ions are followed. For each guiding-center particle, 64 particles with different gyration phase are traced. Figure 6 is a schematic picture of the numerical FILD. Only fast ions passing through the aperture are detected by the numerical FILD. We see the helical symmetry in the lost fast-ion location shown in Figs. 3 and 4. Though the AEs and the beam deposition location do not have the helical symmetry and we need the whole-device simulations, the
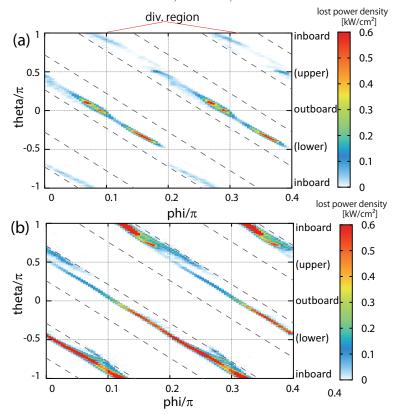
FIGURE 4. Spatial distributions of increment in the power density of lost fast ions for (a) co-going fast ions and (b) counter-going fast ions. The horizontal and vertical axes are the toroidal angle and poloidal angle of lost fast-ion location, respectively. Color represents the increment in the power density of lost fast ion [kW/cm^2]. In these Figs, the spatial distribution of lost fast ions is shown for $0 \leqslant \phi \leqslant 2\pi/5$ (two helical pitch).

AEs and fast ions propagate in both poloidal and toroidal directions. Our interpretation is that the asymmetric effects of the AEs and the beam deposition location are smoothed out during their propagation leading to the helical symmetry in the lost fast-ion location. Then, we expect the approximate helical symmetry also for the FILD measurements and set ten numerical FILDs in the helically symmetric locations to reduce the Monte Carlo error.

3.2.2. *Comparison between numerical FILD and FILD measurements*

The numerical FILD is introduced to the fast-ion loss simulation with MEGA code, and the velocity distribution of lost fast ions is investigated with the numerical FILD. Figure 7 compares the numerical FILD measurement for the pitch-angle and energy distributions of lost fast ions during the AE burst with the FILD measurement in the LHD. The lost fast-ion measurements of FILD shown in Fig. 7(c) were published in Ref. Ogawa et al. (2012). In Fig. 7(a), fast ions with energy close to the injection energy are mainly detected by the numerical FILD before the AE bursts. During the AE burst, we see in Fig. 7(b) that fast ions of 100-150 keV and 35-50 degree are detected by the numerical FILD. In the previous comparison, the energy of fast ion detected is only near the injection energy(Ogawa et al. 2012). The velocity space region of the lost fast ions due to the AE burst is in good agreement with that observed in the experiment shown
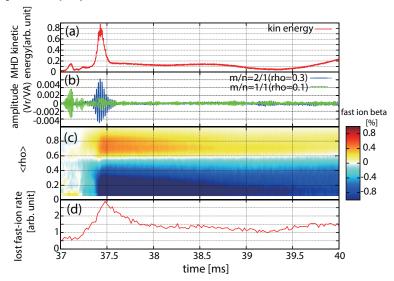
FIGURE 5. Time evolutions of (a) MHD kinetic energy, (b) mode amplitudes with $m/n = 2/1$ and $m/n = 1/1$, (c) fast-ion pressure profile variation, and (d) fast-ion loss rate during a burst of fast-ion driven instabilities. In panel (c) color represents the difference of fast-ion pressure from that before the AE burst at t=37 ms. In panel (d), fast-ion loss rate does not include the promptly lost particles whose lifetime is less than 50 μs.
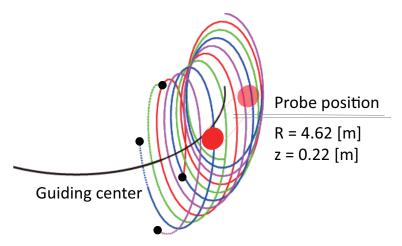

FIGURE 6. Model of the numerical FILD for LHD.

in Fig. 7(c), although the two peaks observed in the experiment are not well resolved in the numerical FILD. This discrepancy can be attributed to the aperture size of the numerical FILD which is about five times larger than that of the FILD in the experiment. Therefore, the fast ions with the wider range of pitch angle and energy may be detected by the numerical FILD than those detected by the FILD in the experiment. In Ref. Ogawa et al. (2012), it was shown that the lost fast ion with pith angle = 30-40 degree detected by the FILD increased during the AE burst. The numerical FILD measurement is consistent with the experiment for the lost fast ions with pith angle = 30-40 degrees. Most of the fast ions detected are re-entering fast ions which re-enter the plasma after passing through outside of plasma(Seki et al. 2008). These re-entering fast ions are not
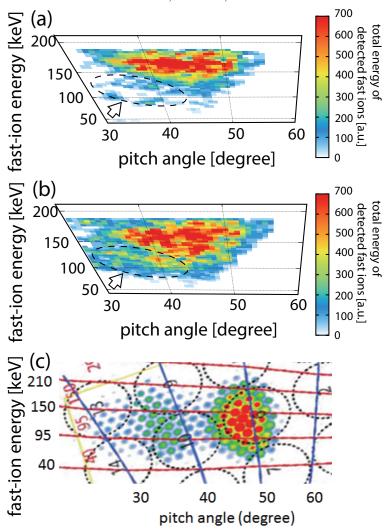
FIGURE 7. Comparison of pitch-angle and energy distribution of lost fast ions among (a) MEGA simulation before AE burst, (b) MEGA simulation during AE burst, and (c) FILD measurements during AE burst. Color represents the total energy of the detected fast ions [arb.unit]. The lost fast-ion measurements with FILD shown in Fig. (c) were published in Ref. Ogawa et al. (2012).

directly lost in the divertor region. The difference between the fast ions detected by the "numerical FILD" and the lost fast ions to the divertor region is discussed in Sec. 3.3.

3.3. Comparison between fast ions detected by numerical FILD and fast ions lost to divertor region

We examined the fast ions lost to the divertor region during the AE burst(Seki et al. 2019). Here, we investigate the difference between fast ions detected by the numerical FILD, in which co-going fast ion are mainly detected, and co-going fast-ion lost to the divertor region. Figure 8 compares the radial deposition profiles of the lost fast ions detected by the numerical FILD and the lost fast ions to the divertor region. In this simulation, the AE burst occurs at $t = 37.4$ ms as shown in Fig. 5. In Fig. 8(b), the deposition points of co-going fast ions lost to the divertor region are located up to the

plasma center before the AE burst as well as during the AE burst. During the AE burst, the loss of co-going fast ions with the deposition point near the peripheral region increases significantly. On the other hand, most of the fast ions detected by the numerical FILD are the fast ions deposited near rho ~ 0.9 even before the AE burst. This is because most of fast ions detected by the numerical FILD are re-entering particles. In the numerical FILD, the fast ions deposited up to rho ~ 0.7 are detected only during the AE burst. This result indicates that fast ions which are transported to the peripheral region of the plasma during the AE burst are detected. Figure 9 compares the time evolutions of energy distribution of the lost fast ions detected by the numerical FILD and the lost fast ions to the divertor region. In this simulation, there is a clear difference in energy distribution between the fast ions detected by the numerical FILD and the fast ions lost to the divertor region. Before the AE burst, fast ions with high energy (150-180 keV) close to the beam injection energy (~ 180 keV) are mainly detected by the numerical FILD. During the AE burst, fast ions with middle energy (100-150 keV) are detected by the numerical FILD in addition to the high-energy particles with 150-180 keV. On the other hand, the main component of co-going fast-ions lost to the divertor region are the particles with energy lower than 50 keV. This difference between the fast ions detected by the numerical FILD and the co-going fast ions lost to the divertor region arises because most of the fast ions detected by the numerical FILD are re-entering fast ions. The re-entering fast ions are not directly lost in the divertor region as mentioned in Sec. 3.2.2.
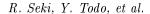
4. Summary

We have conducted the multi-phase simulations with the kinetic-MHD hybrid code MEGA to investigate the spatial and the velocity distributions of lost fast ions due to the AE bursts in the LHD plasmas. We found that fast ions are lost along the divertor region with helical symmetry both before and during the AE burst except for the promptly lost particles. On the other hand, several peaks are present in the spatial distribution of lost fast ions along the divertor region. These peaks along the divertor region can be attributed to the deviation of the fast-ion orbits from the magnetic surfaces due to the grad-B and the curvature drifts.

In order to compare the MEGA simulation with the FILD measurements, the "numerical FILD" which solves Newton-Lorentz equation has been developed and implemented in the MEGA simulation. In the MEGA simulation with "numerical FILD", the velocity space distribution of the lost fast ions due to the AE burst is in good agreement with that observed in the experiment, although the two peaks observed in the experiment are not well resolved in the numerical FILD. This agreement validates the MEGA simulation on the lost fast-ion distribution in the divertor region.

We investigated the difference between the fast ions detected by the numerical FILD and the co-going fast ions lost to the divetor region. In the numerical FILD, co-going fast ion are mainly detected. The deposition points of the co-going fast ions lost to the divertor region are located up to the plasma center before the AE burst as well as during the AE burst. During the AE burst, co-going fast ions with the deposition point near the peripheral region are significantly lost.

On the other hand, most of the fast ions detected by the numerical FILD are fast ions deposited near rho ~ 0.9 even before the AE burst. The main component of the co-going fast ions lost to the divertor region are the particles with lower energy than 50 keV. Most of the lost co-going fast ions to the divertor region are lost after slowing down. On the other hand, before the AE burst, fast ions with high energy (150-180 keV) close to the
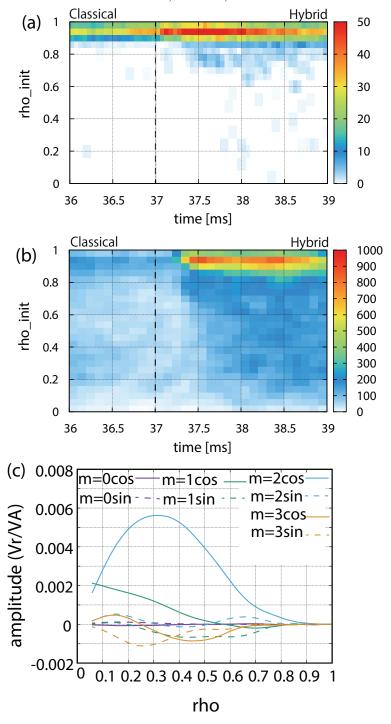
FIGURE 8. Time evolution of the radial deposition profile of (a) fast ions detected by numerical FILD and (b) co-going fast ions lost to the divertor region. Color represents the number of fast ions [arb.unit]. In panel (c), the radial profile of mode amplitude at the maxima of this AE burst are shown for reference. The hybrid phase of the multi-phase simulation is 37 ms-40 ms, and the classical phase where the MHD perturbations are tuned off is 35 ms-37 ms. The AE burst occurs at t=37.4 ms as shown in Fig. 5.
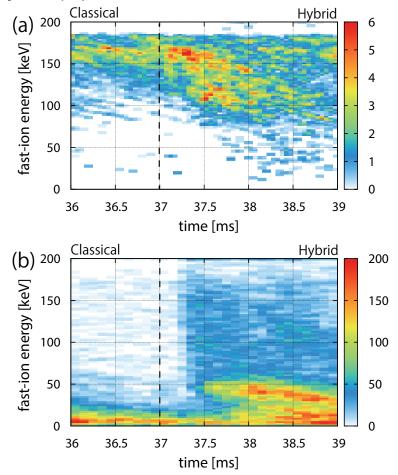
FIGURE 9. Time evolution of energy profile of (a) fast ions detected by the numerical FILD and (b) co-going fast ions lost to the divertor region. Color represents the number of fast-ions [arb. unit]. The hybrid phase of the multi-phase simulation is 37 ms-40 ms, and the classical phase where the MHD perturbations are turned off is 35 ms-37 ms. The AE burst occurs at t=37.4 ms as shown in Fig. 5.

beam injection energy ($\sim$ 180 keV) are mainly detected by the numerical FILD. During the AE burst, fast ions with middle energy (100-150 keV) are detected by the numerical FILD in addition to the high-energy particles with 150-180 keV. These differences can be attributed to the orbits of the fast ions detected by the numerical FILD. The fast ions detected by the (numerical) FILD re-enter the plasma if the (numerical) FILD is not present and are not directly lost in the divertor region.

The discrepancy between numerical FILD and FILD measurment is because the aperture size of numerical FILD is about 5 times larger than that of the actual FILD. In the near future, fast-ion loss will be analyzed by numerical FILD with the aperture close to actual size. The time evolution of fast-ion loss will be calculated by only hybrid simulation. In the LHD, the time evolution of the fast-ion energy distribution associated with the AE burst has been observed with the electric field parallel to the magnetic field type neutral particle analyzer(E∥B-NPA)(Fujiwara et al. 2020). In our future work, the MEGA simulation results will be compared with the E∥B-NPA measurements in order to clarify the nonlinear interaction between fast ions and AEs.

REFERENCES

BIERWAGE, A., SHINOHARA, K., TODO, Y., AIBA, N., ISHIKAWA, M., MATSUNAGA, G., TAKECHI, M. & YAGI, M. 2018 Simulations tackle abrupt massive migrations of energetic beam ions in a tokamak plasma. *Nature communications* **9** (1), 1–11.

BIERWAGE, A. & TODO, Y. 2017 Benchmark of multi-phase method for the computation of fast ion distributions in a tokamak plasma in the presence of low-amplitude resonant mhd activity. *Computer Physics Communications* **220**, 279–284.

BRIGUGLIO, S., VLAD, G., ZONCA, F. & KAR, C. 1995 Hybrid magnetohydrodynamic-gyrokinetic simulation of toroidal alfvén modes. *Physics of Plasmas* **2** (10), 3711–3723.

BURBY, J. W. & TRONCI, C. 2017 Variational approach to low-frequency kinetic-mhd in the current coupling scheme. *Plasma Physics and Controlled Fusion* **59** (4), 045013.

FU, G., PARK, W., STRAUSS, H., BRESLAU, J., CHEN, J., JARDIN, S. & SUGIYAMA, L. 2006 Global hybrid simulations of energetic particle effects on the n= 1 mode in tokamaks: Internal kink and fishbone instability. *Physics of plasmas* **13** (5), 052517.

FUJIWARA, Y., KAMIO, S., OGAWA, K., YAMAGUCHI, H., SEKI, R., NUGA, H., NISHITANI, T., ISOBE, M. & OSAKABE, M. 2020 Enhancement of an e parallel b type neutral particle analyzer with high time resolution in the large helical device. *Journal of Instrumentation* **15** (02), C02021.

HARAFUJI, K., HAYASHI, T. & SATO, T. 1989 Computational study of three-dimensional magnetohydrodynamic equilibria in toroidal helical systems. *Journal of computational physics* **81** (1), 169–192.

METT, R. & MAHAJAN, S. 1992 Kinetic theory of toroidicity-induced alfvén eigenmodes. *Physics of Fluids B: Plasma Physics* **4** (9), 2885–2893.

NISHIMURA, S., TODO, Y., SPONG, D. A., SUZUKI, Y. & NAKAJIMA, N. 2013 Simulation study of alfvén-eigenmode-induced energetic ion transport in lhd. *Plasma and Fusion Research* **8**, 2403090–2403090.

NÜHRENBERG, C. 1999 Compressional ideal magnetohydrodynamics: Unstable global modes, stable spectra, and alfvén eigenmodes in wendelstein 7–x-type equilibria. *Physics of Plasmas* **6** (1), 137–147.

OGAWA, K., ISOBE, M., TOI, K., SPONG, D. A., OSAKABE, M., GROUP, L. E. & OTHERS 2012 Magnetic configuration effects on tae-induced losses and a comparison with the orbit-following model in the large helical device. *Nuclear Fusion* **52** (9), 094013.

OSAKABE, M., YAMAMOTO, S., TOI, K., TAKEIRI, Y., SAKAKIBARA, S., NAGAOKA, K., TANAKA, K., NARIHARA, K., GROUP, L. E. & OTHERS 2006 Experimental observations of enhanced radial transport of energetic particles with alfvén eigenmode on the lhd. *Nuclear fusion* **46** (10), S911.

PARK, W., PARKER, S., BIGLARI, H., CHANCE, M., CHEN, L., CHENG, C.-Z., HAHM, T., LEE, W., KULSRUD, R., MONTICELLO, D. & OTHERS 1992 Three-dimensional hybrid gyrokinetic-magnetohydrodynamics simulation. *Physics of Fluids B: Plasma Physics* **4** (7), 2033–2037.

PINON, J., TODO, Y. & WANG, H. 2018 Effects of fast ions on interchange modes in the large helical device plasmas. *Plasma Physics and Controlled Fusion* **60** (7), 075007.

SATO, M. & TODO, Y. 2019 Effect of precession drift motion of trapped thermal ions on ballooning modes in helical plasmas. *Nuclear Fusion* **59** (9), 094003.

SEKI, R., MATSUMOTO, Y., SUZUKI, Y., WATANABE, K. & ITAGAKI, M. 2008 Particle orbit analysis in the finite beta plasma of the large helical device using real coordinates. *Plasma and Fusion Research* **3**, 016–016.

SEKI, R., TODO, Y., SUZUKI, Y., SPONG, D., OGAWA, K., ISOBE, M. & OSAKABE, M. 2019 Comprehensive magnetohydrodynamic hybrid simulations of alfvén eigenmode bursts and fast-ion losses in the large helical device. *Nuclear Fusion* **59** (9), 096018.

SPONG, D., CARRERAS, B. & HEDRICK, C. 1992 Linearized gyrofluid model of the alpha-destabilized toroidal alfvén eigenmode with continuum damping effects. *Physics of Fluids B: Plasma Physics* **4** (10), 3316–3328.

SUZUKI, Y., NAKAJIMA, N., WATANABE, K., NAKAMURA, Y. & HAYASHI, T. 2006 Development and application of hint2 to helical system plasmas. *Nuclear fusion* **46** (11), L19.

Todo, Y. 2016 Multi-phase hybrid simulation of energetic particle driven magnetohydrodynamic instabilities in tokamak plasmas. *New Journal of Physics* **18** (11), 115005.

Todo, Y. 2019 Critical energetic particle distribution in phase space for the alfvén eigenmode burst with global resonance overlap. *Nuclear Fusion* **59** (9), 096048.

Todo, Y., Murakami, S., Yamamoto, T., Fukuyama, A., Spong, D. A., Yamamoto, S., Osakabe, M. & Nakajima, N. 2010a Numerical analyses of energetic particles in lhd. *Fusion Science and Technology* **58** (1), 277–288.

Todo, Y., Nakajima, N., Sato, M. & Miura, H. 2010b Simulation study of ballooning modes in the large helical device. *Plasma and Fusion Research* **5**, S2062–S2062.

Todo, Y. & Sato, T. 1998 Linear and nonlinear particle-magnetohydrodynamic simulations of the toroidal alfvén eigenmode. *Physics of plasmas* **5** (5), 1321–1327.

Todo, Y., Sato, T., Watanabe, K., Watanabe, T. & Horiuchi, R. 1995 Magnetohydrodynamic vlasov simulation of the toroidal alfvén eigenmode. *Physics of Plasmas* **2** (7), 2711–2716.

Todo, Y., Seki, R., Spong, D., Wang, H., Suzuki, Y., Yamamoto, S., Nakajima, N. & Osakabe, M. 2017 Comprehensive magnetohydrodynamic hybrid simulations of fast ion driven instabilities in a large helical device experiment. *Physics of plasmas* **24** (8), 081203.

Todo, Y., Van Zeeland, M., Bierwage, A. & Heidbrink, W. 2014 Multi-phase simulation of fast ion profile flattening due to alfvén eigenmodes in a diii-d experiment. *Nuclear Fusion* **54** (10), 104012.

Todo, Y., Van Zeeland, M., Bierwage, A., Heidbrink, W. & Austin, M. E. 2015 Validation of comprehensive magnetohydrodynamic hybrid simulations for alfvén eigenmode induced energetic particle transport in diii-d plasmas. *Nuclear Fusion* **55** (7), 073020.

Todo, Y., Van Zeeland, M. & Heidbrink, W. 2016 Fast ion profile stiffness due to the resonance overlap of multiple alfvén eigenmodes. *Nuclear Fusion* **56** (11), 112008.

Wang, H., Todo, Y., Ido, T., Suzuki, Y. & others 2018 Chirping and sudden excitation of energetic-particle-driven geodesic acoustic modes in a large helical device experiment. *Physical review letters* **120** (17), 175001.

Wang, H., Todo, Y., Oasakabe, M., Ido, T. & Suzuki, Y. 2019 Simulation of energetic particle driven geodesic acoustic modes and the energy channeling in the large helical device plasmas. *Nuclear Fusion* **59** (9), 096041.

Wang, X., Zonca, F. & Chen, L. 2010 Theory and simulation of discrete kinetic beta induced alfvén eigenmode in tokamak plasmas. *Plasma Physics and Controlled Fusion* **52** (11), 115005.